

Spin polarization regulates photocatalytic CO₂ into hydrocarbons by Co doped BiOCl

Wenjuan Li ^a, Yipin Zhang ^a, Weiguang Ran ^a, Yuhua Wang ^a, Fu Tian ^a, Fuzhi Zhang ^a, Min Xu ^a, Dapeng Zhang ^a, Na Li ^a, Tingjiang Yan ^{a,b,*}

^a Key Laboratory of Catalytic Conversion and Clean Energy in Universities of Shandong Province, School of Chemistry and Chemical Engineering, Qufu Normal University, Qufu 273165, PR China

^b College of Chemistry and Chemical Engineering, Shaanxi University of Science and Technology, Xi'an 710021, PR China

ARTICLE INFO

Keywords:
Spin polarization
Co
CO₂ hydrogenation
Hydrocarbon

ABSTRACT

Doping magnetic elements into semiconductors is an effective strategy for manipulating spin-polarized electrons in photocatalysis. This work indicates that the introduction of spin-polarized electrons into BiOCl ultrathin sheets remarkably boosts the efficiency of photocatalytic CO₂ reduction by doping BiOCl with magnetic Co. The Co-doped BiOCl (Co-BiOCl) photocatalyst selectively converts CO₂ into CH₄ and C₂₊ products with a hydrocarbon selectivity of 76.9 %, which is not available for pristine BiOCl. The spin-polarized electrons generated from Co-BiOCl promote CO adsorption, stabilize the key CO* intermediate, and significantly reduce the kinetic barrier to CH₂* formation, tuning the subsequent hydrogenation and C–C coupling into hydrocarbons. The regulatory effect of spin polarization on photocatalytic CO₂ reduction can also be observed for Fe-, Ni- or non-magnetic element Cu- doped BiOCl. Hence, this work provides new insight into the regulation of the photoreduction of CO₂ to hydrocarbon products by spin-polarized electrons.

1. Introduction

Solar-driven photocatalytic conversion of CO₂ into valuable chemicals is a promising strategy for addressing the problems of energy shortages and climate change [1,2]. However, because photocatalytic CO₂ reduction is a complicated multielectron transfer process, designing suitable photocatalysts for improving the efficiency of CO₂ reduction, especially for photocatalytic CO₂ into hydrocarbons, is still a great challenge. Taking the simplest CH₄ hydrocarbon product as an example, from a kinetic point of view, the formation of CH₄, which requires eight electrons, is more difficult than the two-electron reduction of CO₂ to CO [3]. Although some impressive photocatalysts were designed for CO₂ photoreduction to CH₄, including CuIn₅S₈, C-In₂O₃, Au-ZnIn₂S₄, MOF-808-CuNi, and CeCo-poly(triazine imide) [3–7], the conversion efficiency of CO₂ into hydrocarbons is still limited, which can be attributed to the high chemical inertness of linear CO₂ molecules and the rapid recombination of photogenerated charge carriers [8,9]. Therefore, it is imperative to pursue efficient strategies to promote CO₂ adsorption and charge separation and transport.

As reported, BiOCl is a promising photocatalyst for CO₂ reduction, due to its unique layered structures, which are composed of a bismuth oxygen layer and a chloride ion layer, allowing for the capture of sunlight due to refraction between layers under incident light [10–12]. The special characteristics of BiOCl have attracted extensive attention in CO₂ reduction [13–16]. However, BiOCl still suffers from low photocatalytic activity and conversion efficiency because of its limited ability to adsorb CO₂, and poorly activate CO₂ [13–16]. To solve these problems, diverse studies on BiOCl-based photocatalytic reduction of CO₂ have been carried out, such as defect engineering, element doping, crystal facet engineering, and heterojunction construction [17–23]. For example, BiOCl nanoflowers with high oxygen vacancies (Ovs) levels for photocatalytic CO₂ reduction promoted the electron recruitment of photogenerated electrons, resulting in more active sites, and thus increasing the CO yield [17]. Cu modification promoted the photocatalytic CO₂ reduction reaction over BiOCl nanosheets, leading to remarkable photocatalytic CO₂ reduction activity and achieving a 50 % improvement compared to that of pristine BiOCl [18]. A rose-like BiOCl material rich in Bi vacancies assembled from fully exposed active {001} facets on nanosheets

* Corresponding author at: Key Laboratory of Catalytic Conversion and Clean Energy in Universities of Shandong Province, School of Chemistry and Chemical Engineering, Qufu Normal University, Qufu 273165, PR China.

E-mail address: tingjiang@163.com (T. Yan).



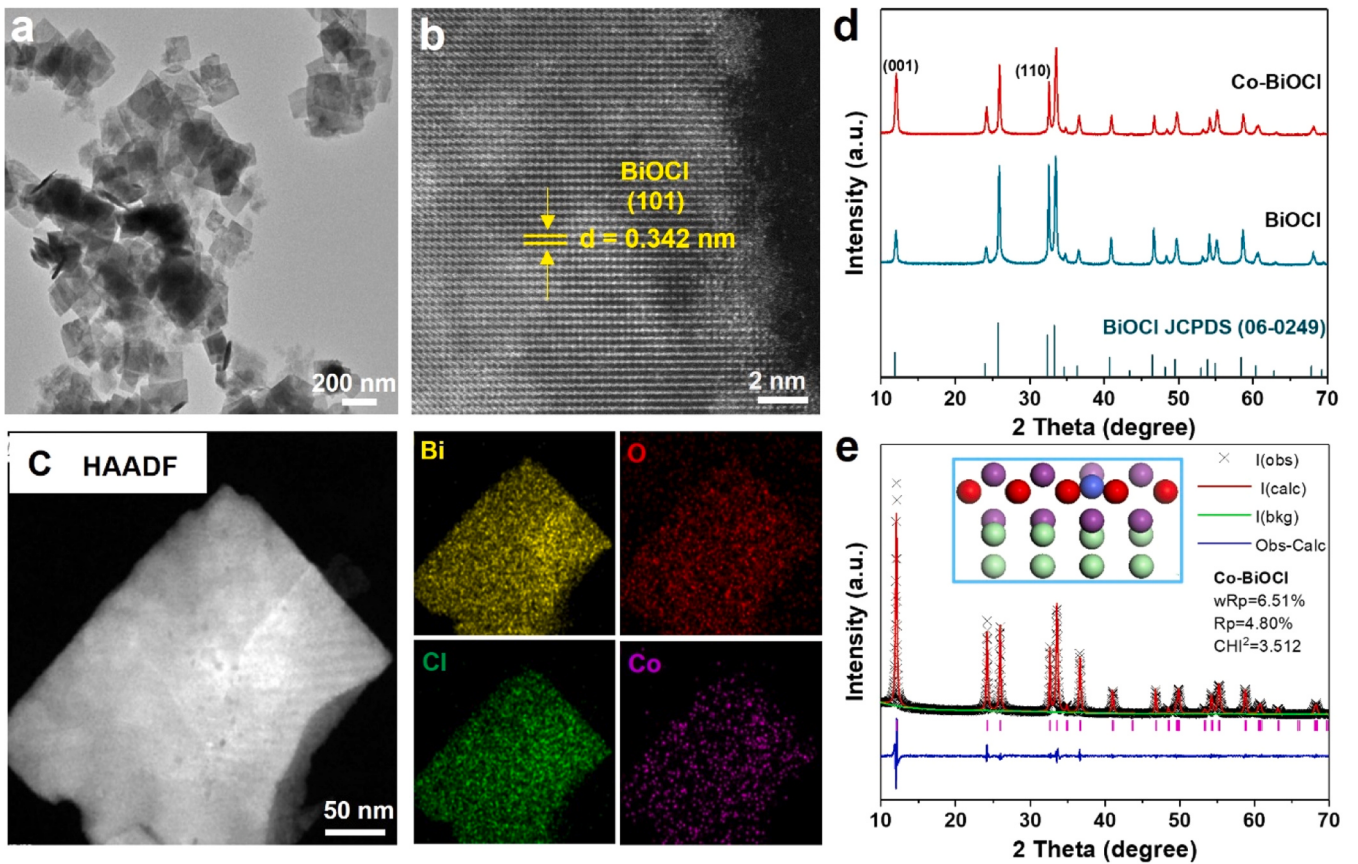


Fig. 1. (a, b) TEM images and (c) atomic resolution HAADF–STEM and EDS mapping images of Bi, O, Cl, and Co of Co-BiOCl. (d) XRD patterns of Co-BiOCl and pristine BiOCl. (e) Crystal structure refinement of Co-BiOCl (The inset is the DFT structure of Co-BiOCl. Blue, purple, red and green atoms stand for Co, Bi, O, Cl).

provided considerable adsorption and catalytic sites for CO_2 capture and reduction, thus accelerating CO generation [19]. By fabricating a Bi-BiOCl/MgIn₂S₄ heterostructure, CO_2 photoreduction into methane was achieved [20]. Among these reports, most have focused on reducing CO_2 to CO, and few have focused on reducing CO_2 to hydrocarbons. According to the characteristics of CO_2 reduction, the preparation of desirable hydrocarbon compounds from CO_2 requires overcoming the activation of C=O bonds and the coupling of C–C bonds kinetically, which requires sufficient photoinduced electrons to participate in the photocatalytic reduction process [24,25]. Accelerating the separation of charge carrier and the transport of electrons to increase the number of electrons is deemed effective for converting CO_2 into hydrocarbon fuels. Recent reports indicate that the spin polarization of photoexcited electrons has a positive impact on enhancing charge separation, suppressing charge recombination, and thus promoting the photocatalytic activities of materials [26–28]. For instance, the introduction of Mn²⁺ doping to manipulate spin-polarized electrons in CsPbBr₃ halide perovskite nanoplates can enhance the photocatalytic CO_2 reduction reaction [26]. The spin-state transition of cobalt (Co) in covalent organic frameworks (COFs) profoundly regulates the performance of photocatalytic CO_2 reduction, resulting in favorable activity and significantly improved selectivity for HCOOH [27]. The spin transition of the catalytic active sites Fe³⁺ significantly enhances orbital overlap between specific substrates and the catalyst. Consequently, the ultrathin metal–organic layer catalyst, which incorporates the Fe³⁺ catalytic center, leads to markedly increased activity and selectivity for CO_2 photoreduction [28]. Therefore, the regulation of electronic spin state as well as the intrinsic characteristic property of electrons through the incorporation of magnetic elements into semiconductors, has achieved good performance in the photocatalytic field [26].

Co, Fe and Ni are the most common metallic ions to be doped into BiOCl semiconductors for boosting the photocatalytic activity [29–33]. In particular, Co is one of the most effective doping species, which can broaden the light absorption range and improve the charge separation of BiOCl, thereby restraining the recombination of photo-generated carriers [29–31]. For example, Co doped BiOCl exhibited 3.5 times higher photocatalytic activity than that of BiOCl towards the degradation of bisphenol A [29]. Co doped and oxygen vacancy contained BiOCl exhibited extremely high photocatalytic efficiency of 98.9 % for degrading organic pollutants and reducing Cr(VI) [30]. Co-doped BiOCl ultrathin nanosheets displayed enhanced visible-light-driven photocatalytic activity in degrading the persistent contaminant of carbamazepine [31]. However, the photocatalytic enhancement of these Co-BiOCl was mainly focused on the liquid degradation, and few attentions were paid on photocatalytic CO_2 reduction. Furthermore, the effect of spin state of Co doping on the photocatalytic activity has been not concerned yet. In this work, the Co-doped BiOCl (Co-BiOCl) photocatalysts were successfully prepared by a one-step method. The experimental and density functional theory (DFT) results show that the introduction of Co atoms tunes the charge distribution on the BiOCl surface, leading to spin polarization. Due to the spin polarization of the magnetic Co atom, the photocatalytic CO_2 reduction efficiency of Co-BiOCl can be significantly enhanced due to the increased separation rate of photogenerated carriers and suppression of charge recombination. The selective conversion of CO_2 to CH₄ and C₂₊ products over Co-BiOCl under light irradiation was achieved. The selectivity of hydrocarbons on Co-BiOCl can reach 76.9 %, which is not available on pristine BiOCl. Furthermore, the universality of the strategy for activating CO_2 reduction was also exhibited for Fe-, Ni- or non-magnetic element Cu- doped BiOCl. Our study provides a facile and efficient strategy for the selective conversion

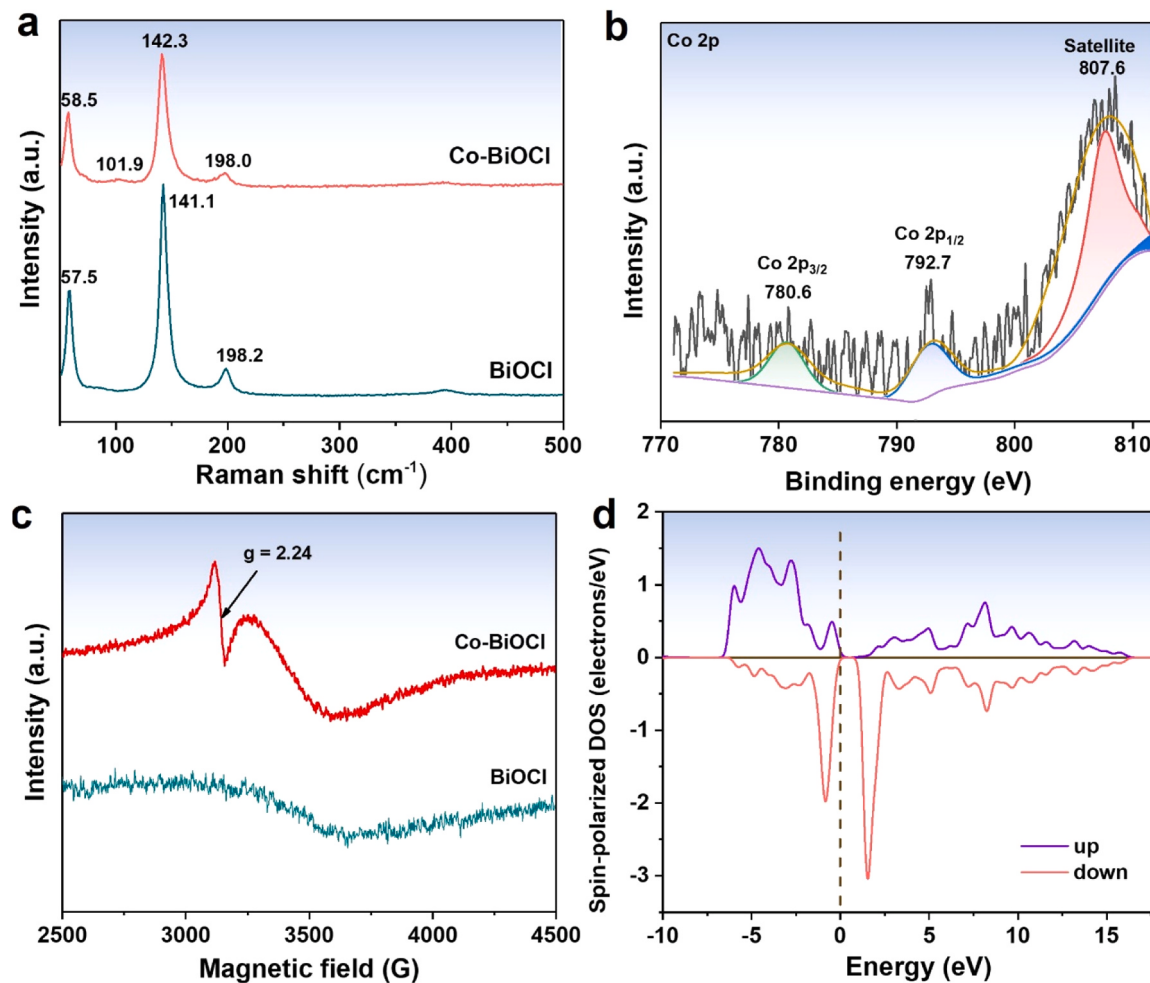


Fig. 2. (a) Raman spectra of pristine BiOCl and Co-BiOCl. (b) XPS of Co 2p in Co-BiOCl. (c) EPR spectra of pristine BiOCl and Co-BiOCl. (d) Spin-polarized DOS of Co-BiOCl.

of CO₂ to hydrocarbon products through spin polarization.

2. Experimental

The detailed information was shown in the [Supporting information](#).

3. Results and discussion

3.1. Effect of Co on the structure of BiOCl

The incorporation of Co atoms into the BiOCl lattice structure was achieved through a straightforward chemical method, as detailed in the [Supporting Information](#). Transmission electron microscopy (TEM, Fig. 1a) and scanning electron microscopy (SEM) images ([Figure S1, Supporting Information](#)) of the resulting Co-BiOCl reveal ultrathin sheets, resembling those of pristine BiOCl ([Figure S2](#)). Fig. 1b displays a distinct lattice spacing of $d = 0.342$ nm, attributed to the (101) facet of BiOCl. Aberration-corrected high-angle annular dark field scanning TEM (HAADF-STEM) and EDS mapping images ([Fig. 1c and S3](#)) confirm the uniform distribution of Bi, O, Cl, and Co on the nanosheets, indicating the successful incorporation of Co species onto the BiOCl ultrathin sheets. [Fig. 1d](#) and S4 depict the X-ray diffraction (XRD) and amplified XRD patterns of both pristine BiOCl and Co-BiOCl. The peaks of these materials are similar and can be attributed to the tetragonal phase of BiOCl (JCPDS no. 06-0249). Notably, the diffraction peaks of Co-BiOCl exhibit slight shifts to higher 2θ values compared to pristine

BiOCl, suggesting that Co²⁺ ions may have replaced Bi³⁺ ions within the BiOCl lattice. Additionally, the introduction of Co atoms alters the growth facet of BiOCl from (110) to (001), with an increase in the intensity of the latter peak. To further confirm the presence of Co dopants, crystal structure refinement of the XRD data was performed using the Rietveld method [34] ([Fig. 1e](#)). The lattice parameters for the Co-BiOCl structure were determined as $a = b = 3.88669$ and $c = 7.36407$. The final refinement results exhibited weighted profiles with $R_p = 4.80\%$, $R_{wp} = 6.51\%$, and $\chi^2 = 3.512$, indicating the absence of detectable impurity phases in the obtained sample. All diffraction peaks could be well-fitted using the Rietveld theoretical model calculated after geometry optimization with the CASTEP program (shown in the inset of [Fig. 1e](#)). Furthermore, when compared to the lattice parameters of the pristine BiOCl structure ([Figure S5](#), $a = b = 3.8878$ and $c = 7.36573$), the parameters for Co-BiOCl are slightly smaller. This reduction in size is attributed to the incorporation of Co atoms, which have a smaller ionic radius (Co²⁺ ion). Therefore, it is reasonable to conclude that Co atoms have indeed been incorporated into the crystal structure of BiOCl. Moreover, the incorporation of Co enhances the growth of the (001) facet of BiOCl, which is typically considered the active crystal facet in photocatalysis [19] and can facilitate the adsorption and reduction of CO₂.

The structural variation of BiOCl before and after Co incorporation was also characterized by Raman spectroscopy, as shown in [Fig. 2a](#). For pristine BiOCl, distinguishable peaks at 57.5, 141.1 and 198.2 cm⁻¹ can be observed, corresponding to the A_{1g}¹ external, A_{1g}² internal and E_g²

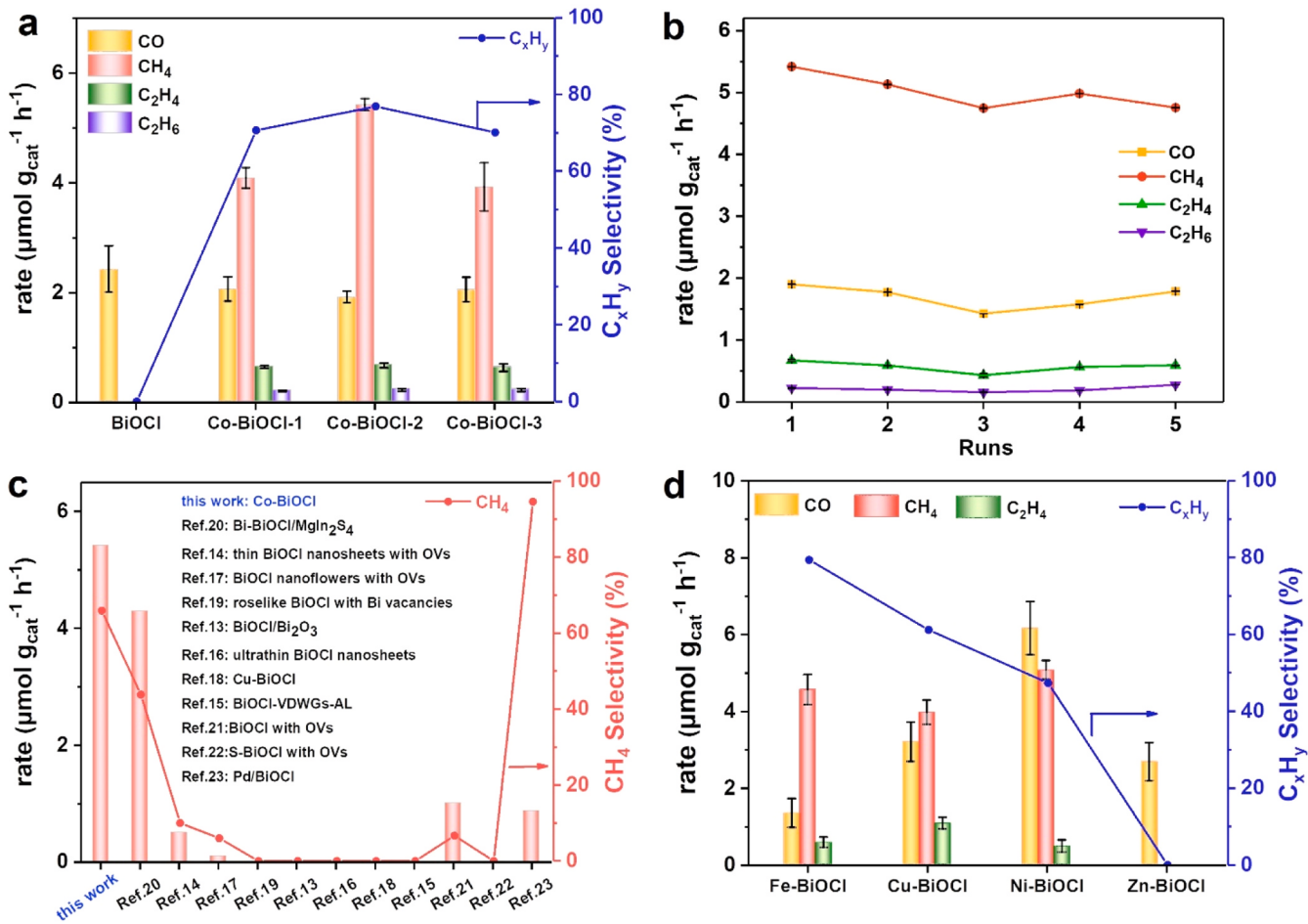


Fig. 3. (a) Photocatalytic CO₂ hydrogenation activity and selectivity of C_xH_y on Co-BiOCl with different Co content after 4 h light irradiation, and (b) cyclic runs of products on Co-BiOCl-2. (c) Comparison of photocatalytic CO₂ hydrogenation activity and CH₄ selectivity on different BiOCl based catalysts in the references [13–23]. (d) Photocatalytic CO₂ hydrogenation activity and selectivity of C_xH_y on Fe-BiOCl, Cu-BiOCl, Ni-BiOCl and Zn-BiOCl.

internal Bi–Cl stretching modes, respectively [35]. Slight right shifts at 58.5 and 142.3 cm⁻¹ are observed for Co-BiOCl, demonstrating that Co doping leads to lattice distortion in BiOCl. Moreover, an additional Raman peak appeared at approximately around 101.9 cm⁻¹ in Co-BiOCl, clearly confirming that the introduced Co–O and Co–Cl bonds affect the lattice periodicity and symmetry of BiOCl [36]. These results further verify that the Co species were successfully incorporated into the BiOCl ultrathin sheets. The existing chemical state of Co in BiOCl was further investigated by X-ray photoelectron spectroscopy (XPS). In Fig. 2b, the high XPS resolution of Co 2p can be deconvoluted into several individual peaks at 792.7 and 807.6 eV, ascribed to Co 2p_{1/2}, and 780.6 eV, ascribed to Co 2p_{3/2}, which are both consistent with the existence of Co²⁺ in BiOCl [37,38]. The binding energies of Bi 4 f, O 2p, and Cl 2p slightly shift after Co²⁺ doping, as shown in Figure S6, indicating that the introduction of Co atoms leads to the inhomogeneous distribution of electron cloud density and the appearance of isolated electron pairs, thus, leading to spin polarization [39]. Electron paramagnetic resonance (EPR) was also utilized to obtain information on the unpaired electrons of Co ions in BiOCl (Fig. 2c). The EPR spectrum of Co-BiOCl shows a strong signal at *g* = 2.24, while this signal does not exist in that of pristine BiOCl, suggesting that unpaired electrons come from Co²⁺ [27,40]. There is also a signal at *g* = 2.04, existing simultaneously in Co-BiOCl and pristine BiOCl, belongs to Ovs on the two samples [41]. DFT calculations were carried out to provide deep insight into spin polarization. As shown in Fig. 2d, Co-BiOCl has opposite and asymmetric spin-polarized density of state (DOS) signals (up/down spin component states), indicating that the incorporation of

Co²⁺ leads to spin polarization in BiOCl [39,40].

3.2. Photocatalytic CO₂ hydrogenation

The CO₂ reduction performance of the as-prepared samples was assessed in a batch reactor under simulated sunlight irradiation, without the addition of any sacrificial reagents. The amount of photocatalyst used in the reduction process was set to 5 mg. As depicted in Fig. 3a, pristine BiOCl nanosheets exhibited a relatively low rate of CO production. However, after incorporating Co, the Co-BiOCl catalysts displayed distinct product distributions, with CH₄ as the primary product and a minor presence of C₂ hydrocarbons (C₂H₄ and C₂H₆). Notably, the Co-BiOCl-2 sample demonstrated the highest level of photocatalytic performance and selectivity for CH₄ (65.9 %, Figure S7). The overall photocatalytic selectivity for hydrocarbons (C_xH_y) reached 76.9 %. As normalized by BET surface areas, the conversion rate of Co-BiOCl-2 was still higher than pristine BiOCl (Figure S8), indicating the negligible effect of texture structure. The Co content was also proved to play minimal role for the photocatalytic CO₂-to-CH₄ conversion (Table S1, Supporting information). In the following, Co-BiOCl-2 sample was chosen as the object to be discussed in detail, designated as Co-BiOCl. Furthermore, control experiments, including CO₂ with photocatalysts without illumination, CO₂ with illumination in the absence of photocatalysts, N₂ with photocatalyst and illumination, and N₂ with illumination in the absence of photocatalysts, were conducted. In all cases, no carbon products were detected, confirming that the conversion of CO₂ molecules into the desired products resulted from photochemical

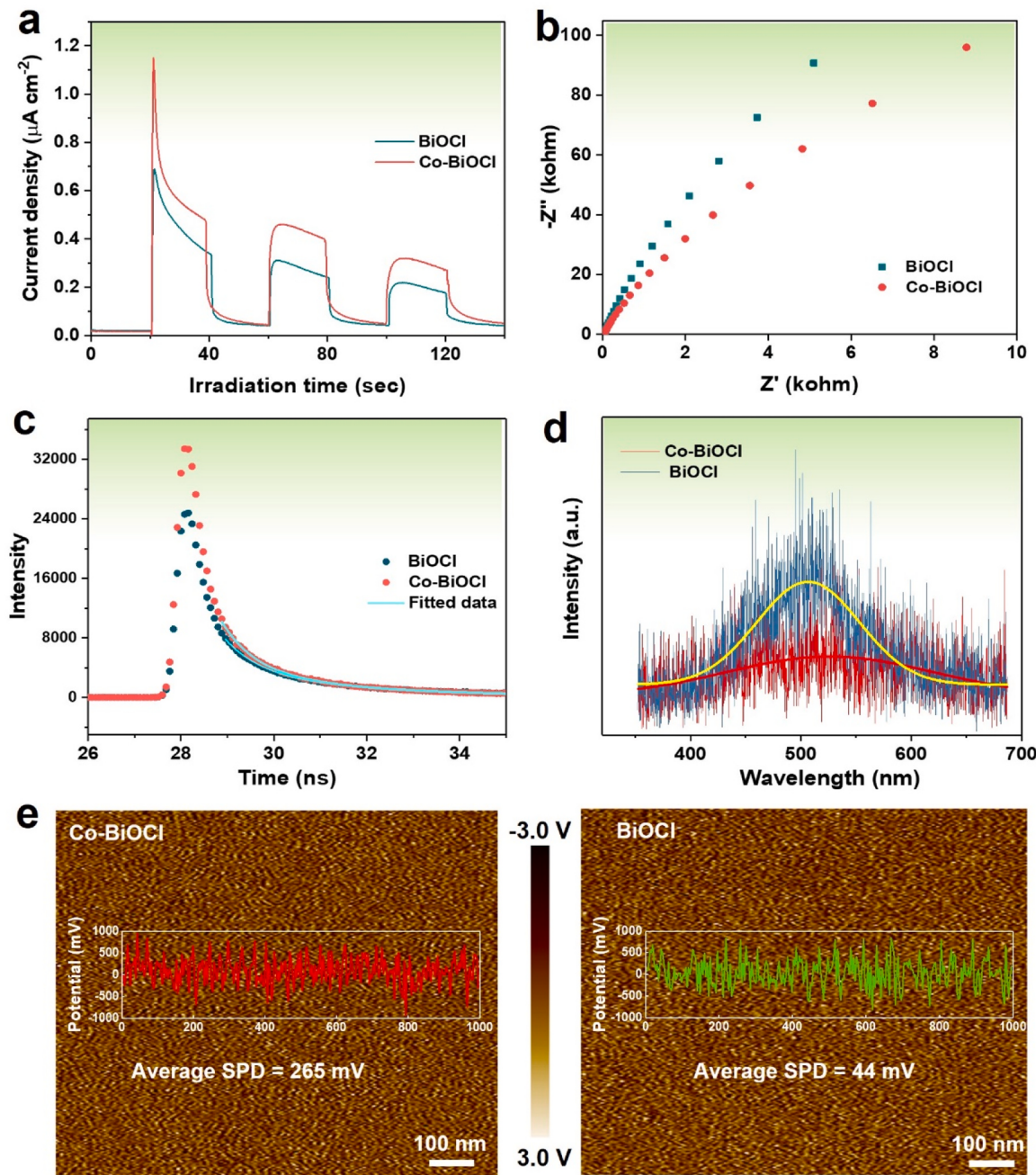


Fig. 4. (a) Transient photocurrent response curves, (b) EIS Nyquist plots without any bias potential, (c) transient-state photoluminescence and (d) steady-state photoluminescence of Co-BiOCl and pristine BiOCl. (e) Average surface potential distribution (SPD) images ($1 \mu\text{m} \times 1 \mu\text{m}$) of Co-BiOCl and pristine BiOCl by KPFM characterization.

reactions rather than residual organics. The durability of Co-BiOCl was evaluated by a sequential cycling test (Fig. 3b). During five consecutive cycles (4 h per cycle), the activity was preserved at a certain stable state. Further characterization, including XPS, TEM, XRD and EPR confirmed the good structural and compositional properties of the Co-BiOCl (Figure S9 and 10), indicating its good structural stability. Moreover, compared with recently reported BiOCl-based photocatalysts [13–23], Co-BiOCl was used for the simultaneous generation of CH_4 and C_{2+} hydrocarbons for the first time, and the Co-BiOCl catalyst exhibited state-of-the-art photocatalytic performance in regulating the photocatalytic reduction of CO_2 into hydrocarbons, as shown in Fig. 3c. These hydrocarbon products always need more electrons than CO, so the introduction of Co is predicted to accelerate carrier transfer and accumulate sufficient electrons in reduction reactions. We also explored the

photoreduction of CO_2 by H_2 on other metal-BiOCl photocatalysts, such as Fe, Ni, and non-magnetic element Cu, which also have spin polarization (Figure S11 and S12). From Fig. 3d, CH_4 also became the main product in the three samples, similar to Co-BiOCl. In comparison, when Zn atoms without spin polarization (Figure S13) were doped on BiOCl, Zn-BiOCl could no longer produce CH_4 and C_{2+} hydrocarbons. Furthermore, the photocatalytic enhancement effect also exhibited on Co-BiOBr system (Figure S14), indicating spin polarization of Co also existed in Co-BiOBr. Based on the above results, spin polarization has a critical influence on the selective photoreduction of CO_2 to CH_4 and C_{2+} hydrocarbons on these metal-BiOCl (or BiOBr)-based photocatalysts.

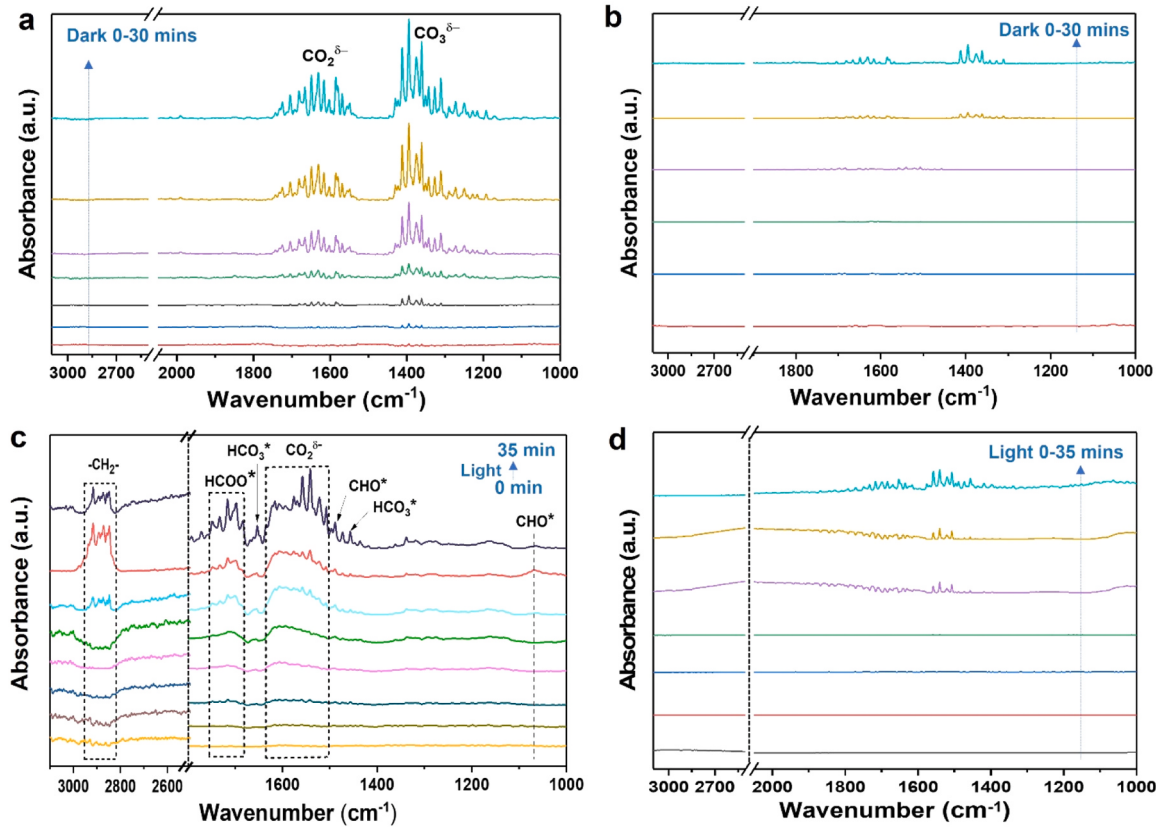


Fig. 5. *In situ* DRIFTS for CO_2 adsorption on (a) Co-BiOCl and (b) pristine BiOCl in dark. *In situ* DRIFTS during the photocatalytic process on (c) Co-BiOCl and (d) pristine BiOCl under light irradiation conditions.

3.3. Mechanism of photocatalytic CO_2 reduction

To elucidate the origin of the enhanced activity and the reaction mechanism for photocatalytic CO_2 reduction, UV–Vis diffuse reflectance spectroscopy (DRS) was performed on both pristine BiOCl and Co-BiOCl samples, as presented in Figure S15. Pristine BiOCl displayed strong absorption solely in the UV region, with an absorption edge at around 344 nm. After incorporating Co, the light absorption intensity of the Co-BiOCl sample was significantly enhanced. Moreover, the calculated bandgap (E_g) from the DRS spectra was 3.26 eV for Co-BiOCl, which is slightly smaller than that of pristine BiOCl (3.32 eV), indicating improved light absorption by the photocatalysts [42]. Mott–Schottky plot analysis (Figure S16) revealed flat-band positions of -0.27 eV for Co-BiOCl and -0.1 eV for pristine BiOCl, resulting in conduction band (CB) energies of -0.37 eV for Co-BiOCl and -0.2 eV for BiOCl. The CB of Co-BiOCl exhibited an upward shift tendency, indicating a greater ability for the reduction of photogenerated electrons and, consequently, facilitating CO_2 photoreduction.

To investigate the photocatalytic mechanism of Co-BiOCl, several techniques were employed to assess photogenerated charge separation/transfer. Fig. 4a shows that Co-BiOCl exhibited a higher transient photocurrent (TPC) density than pristine BiOCl, indicating more efficient photogenerated charge separation. The electrochemical impedance spectroscopy (EIS) spectra (Fig. 4b) of Co-BiOCl displayed a smaller semicircle radius in the Nyquist plot, along with decreased charge-transfer resistance compared to pristine BiOCl, confirming a higher charge carrier transfer rate in Co-BiOCl. Upon fitting the transient-state photoluminescence (PL) curves in Fig. 4c, it was found that the lifetimes of charge carriers for Co-BiOCl ($\tau = 6.80$ ns) exceeded those for pristine BiOCl ($\tau = 3.57$ ns), indicating that charge carriers had sufficient time to participate in the reaction. Additionally, the steady-state photoluminescence (PL) intensity for Co-BiOCl was lower than that for

pristine BiOCl (Fig. 4d), suggesting that Co incorporation suppressed charge-carrier recombination. These results collectively provide evidence that Co sites play a crucial role in influencing charge separation and transfer. Furthermore, a microcosmic analysis revealed that the charge separation and transfer were influenced by the built-in electric field of the sample, as determined by the Kelvin Probe Force Microscope (KPFM) technique. Fig. 4e and S17 demonstrated that Co-BiOCl exhibited a larger average surface potential distribution (SPD) (265 mV) than pristine BiOCl (44 mV), indicating a stronger built-in electric field in Co-BiOCl, which significantly facilitated charge separation and transfer on Co-BiOCl [43].

In addition to charge transfer, the adsorption and activation of CO_2 molecules on catalysts are critical steps in photocatalytic CO_2 reduction. The difference in specific surface areas between pristine BiOCl and Co-BiOCl was minimal (Table S2), suggesting that specific surface area was not the primary factor responsible for the improved physical adsorption of CO_2 . *In situ* diffuse reflectance infrared Fourier-transform spectra (DRIFTS) for CO_2 adsorption on Co-BiOCl (Fig. 5a) revealed peaks at 1630 and 1395 cm^{-1} with increasing adsorption time. The peak at 1630 cm^{-1} was attributed to $\text{CO}_2^{\delta-}$ resulting from CO_2 adsorption at the Co^{2+} site of the $\text{Co}-\text{O}$ bond at the Co-BiOCl interface, while the peak at 1395 cm^{-1} was assigned to $\text{CO}_3^{\delta-}$ originating from CO_2 adsorption on the O site of BiOCl [44–47]. The presence of these two stronger peaks implied that the Co^{2+} and O sites at the interface were favored sites for CO_2 adsorption on Co-BiOCl. In contrast, the DRIFTS peaks of pristine BiOCl (Fig. 5b) were much weaker than those of Co-BiOCl, even at longer adsorption times, indicating that Co-BiOCl exhibited greater CO_2 adsorption capacity than pristine BiOCl.

After CO_2 and H_2 were fed into the reaction system and exposed to light irradiation (0–35 min), the *in situ* DRIFTS spectra of Co-BiOCl exhibited various peaks (Fig. 5c). In addition to the peaks corresponding to $\text{CO}_2^{\delta-}$, peaks at 1066 , 1489 , 1456 , and 1654 cm^{-1} are present,

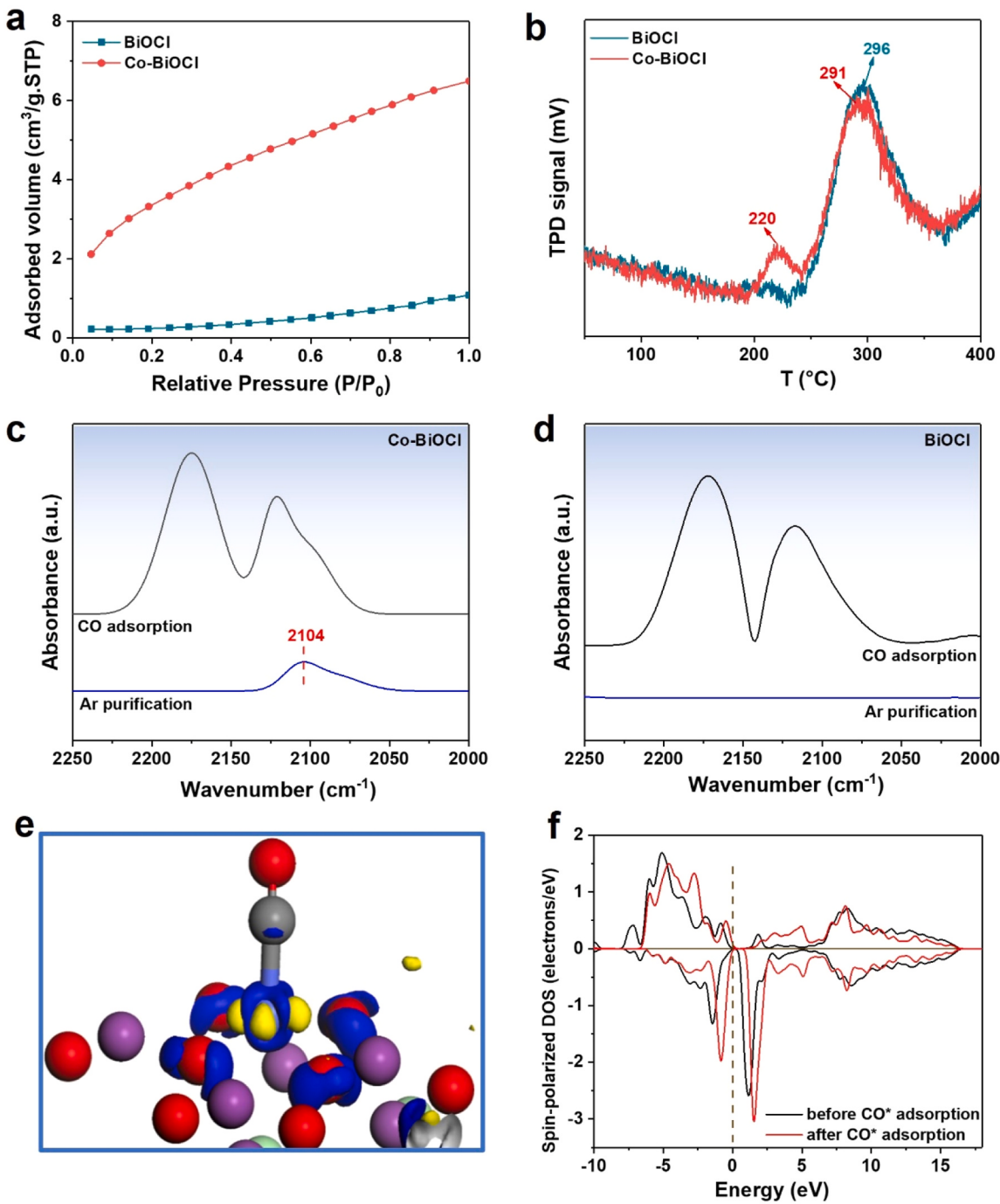


Fig. 6. (a) CO_2 adsorption capacity over Co-BiOCl and pristine BiOCl. (b) CO temperature-programmed desorption curves on Co-BiOCl and pristine BiOCl. *In situ* DRIFTS spectra for CO adsorption on (c) Co-BiOCl and (d) pristine BiOCl. (e) Charge difference distribution of Co-BiOCl after CO^* adsorption, charge accumulation is blue and depletion in yellow. (f) Spin-polarized DOS of Co-BiOCl before and after CO^* adsorption.

assigned to CHO^* and HCO_3^* , respectively, and are important intermediate products of CO_2 photoreduction to CH_4 [48]. The peak at $1683\text{--}1751\text{ cm}^{-1}$ could be attributed to the HCOO^* group, which is also regarded as the crucial intermediate during CO_2 conversion to all the following products [48]. Most importantly, the peak at $2844\text{--}2920\text{ cm}^{-1}$ is attributed to the vibrations of the $-\text{CH}_2-$ groups from the CH_4 and multiple carbon products [49,50], which strongly verifies the generation of C_{2+} hydrocarbons from C–C coupling. Note that, along with the photocatalytic CO_2 hydrogenation, the bands corresponding to the $-\text{CH}_2-$ groups show a trend of initial decrease and then increase, strongly supporting the transformation of carbonate and

bicarbonate intermediate species into CH_4 or C_{2+} hydrocarbon products [49,50]. During the whole reaction process, the peak intensities of the $\text{CO}_2^\delta-$ and HCOO^* groups increase over time, indicating that abundant CO_2 adsorption is the essential origin of photocatalytic reduction. Furthermore, the peak corresponding to $\text{CO}_2^\delta-$ from CO_2 adsorption at the Co^{2+} site of the $\text{Co}-\text{O}$ bond is much stronger and more obvious than the peak corresponding to $\text{CO}_3^\delta-$, which comes from CO_2 adsorption at the O site of BiOCl. This again demonstrated that the Co^{2+} site of the $\text{Co}-\text{O}$ bond on the Co-BiOCl surface plays a major role in CO_2 adsorption and activation. In comparison, the signals of all these species are much weaker than those of pristine BiOCl under the same light irradiation

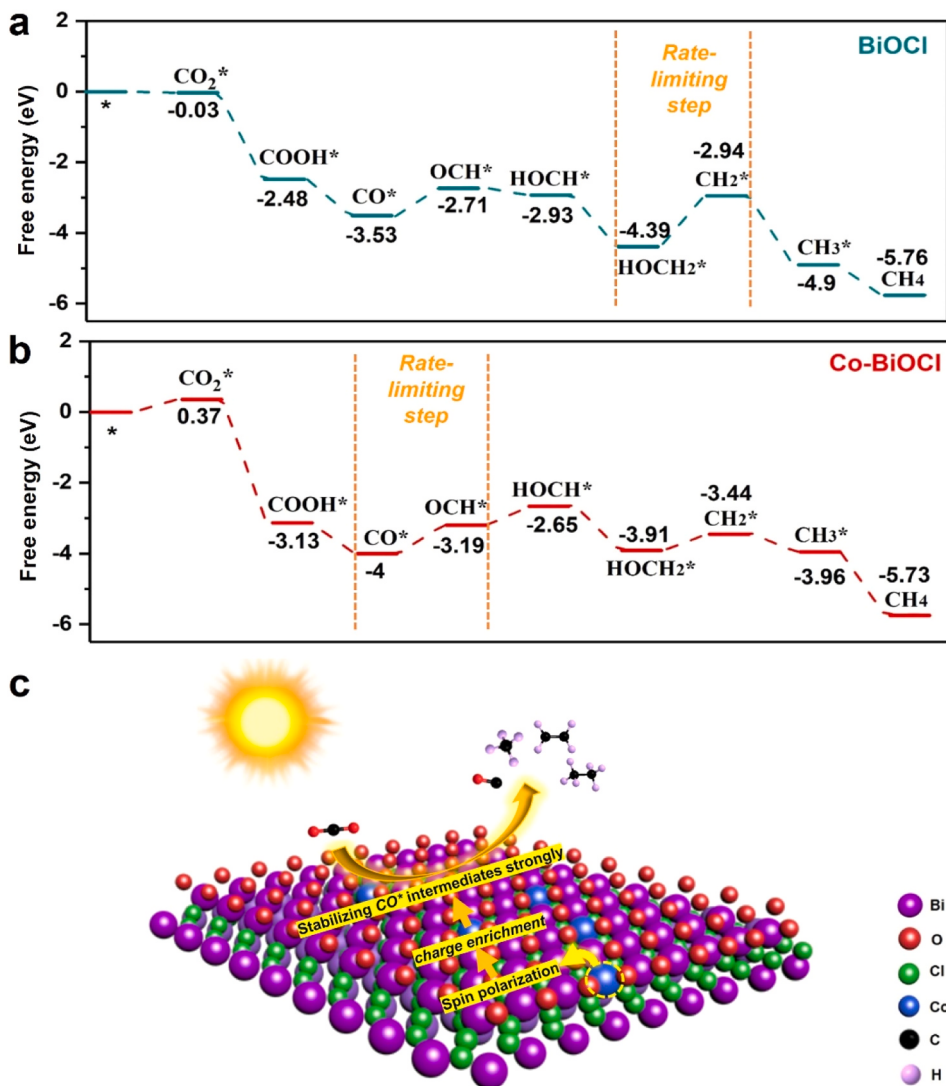


Fig. 7. Computed Gibbs free energy for main reactions in photocatalytic reduction of CO₂ on (a) pristine BiOCl and (b) Co-BiOCl. (c) Advantages of Co-BiOCl for photocatalytic CO₂ reduction.

period (Fig. 5d), in accordance with the photocatalytic performance.

According to the *in situ* DRIFTS spectra, CO₂ photoreduction by H₂ to CH₄ on Co-BiOCl could proceed via a CO₂ → CO₂^Δ → HCOO* → OCH* → CH₂* → CH₄ path. Fig. 6a shows that the CO₂ adsorption capacity of Co-BiOCl is much greater than that of pristine BiOCl. The Mulliken population analysis (Figure S18) indicates that the incorporation of Co affects the charge distribution of Bi and O atoms on the surface of BiOCl, which thereby enables the surface atomic layers to be more negatively charged to absorb CO₂. In the reaction pathway, HCOO* is converted to CO*, with some becoming CO products and some reacting with H to form OCH*. OCH* is an important intermediate in the generation of C₂₊ products, therefore, the surface adsorption of CO is an essential factor. From the CO temperature-programmed desorption curves (Fig. 6b), the first peak at 220 °C is attributed to the physical adsorption of CO. The desorption peak of Co-BiOCl is much stronger than that of BiOCl, indicating more CO molecules were physically adsorbed on the Co-BiOCl sample. The second peak located near 291 °C could be attributed to the chemical adsorption of CO [51]. Compared with pristine BiOCl, the desorption signal of Co-BiOCl became weaker. It indicated that CO was bonded strongly on the Co-BiOCl surface [52], availing for the next hydrogenation to generate CH₄. The DRIFTS results again verified this conclusion. *In situ* DRIFTS was applied to explore CO adsorption on Co-BiOCl and pristine BiOCl (Fig. 6c and d). The experiments involved

two processes: CO adsorption on the samples and then Ar purging to remove the physically adsorbed CO. Compared with the spectrum of pristine BiOCl, the *in situ* DRIFTS spectrum of Co-BiOCl after Ar purification shows a peak at 2104 cm⁻¹ assigned to CO bonding to the Co²⁺ site at the Co-BiOCl interface [44]. The DFT results further verify the electronic interactions between Co-BiOCl and CO. Mulliken population analysis (Figure S18 and S19) of pristine BiOCl, Co-BiOCl, and Co-BiOCl after CO* adsorption indicates that the introduction of Co atoms breaks the charge distribution, and results in spin polarization. The charge difference distribution (Fig. 6e) of Co-BiOCl after CO* adsorption further indicates the strong interaction between Co, O and C atoms, with charge depletion and accumulation occurring mainly at the interface. On the basis of the Mulliken population analysis (Figure S18b and S19), it is concluded that the C atom in CO is charged by Co-BiOCl, which suggests that there is a directional charge transfer from Co to CO near the interface. Moreover, a remarkable shift and increase in the spin-polarized DOS in Co-BiOCl after CO* adsorption can be observed in comparison with that before CO* adsorption (Fig. 6f), especially for the spin-down states of Co, implying that more spin-down states participate in the adsorption process. Therefore, combining the experimental results and theoretical calculations, the introduction of Co increases the spin-polarized charge and enhances CO adsorption on Co-BiOCl. The work function of Co-BiOCl and pristine BiOCl was further estimated

from the energy difference between the vacuum and Fermi levels according to the electrostatic potential of the material by DFT simulation [53]. Theoretical calculations showed that Co-BiOCl (001) has a lower work function than pristine BiOCl (001) (5.36 vs 5.80 eV) (Figure S20), indicating that electrons easily escape from the Co-BiOCl surface to participate in the reaction [54]. This further verifies the role of spin-polarized charges from an indirect view.

To further understand the favorable effect of Co on the generation of CH₄ and C₂₊ hydrocarbons, the changes in free energy during the CO₂ hydrogenation reaction were evaluated for Co-BiOCl and pristine BiOCl. The optimized geometries of the intermediates on the Co-BiOCl (001) and pristine BiOCl (001) surfaces via the minimum energy pathway are shown in Figure S21 and S22. It is generally accepted that the formation of CH₄ and C₂₊ hydrocarbons usually involves the activation of CO₂ to CO* through the COOH* intermediate and the subsequent hydrogenation and coupling of CH* [55,56]. As shown in Fig. 7a, the rate-limiting step of CO₂ hydrogenation on pristine BiOCl is the conversion of HOCH₂* to CH₂*, for which the protonation kinetics barrier is 1.45 eV (derived from 4.39–2.94). In comparison, the rate-limiting step of CO₂ hydrogenation on Co-BiOCl is the conversion of CO* to OCH* (Fig. 7b), for which the protonation kinetics barrier is 0.81 eV (derived from 4–3.19). The energy barrier for the reaction on pristine BiOCl is much greater than that on Co-BiOCl, demonstrating that the introduction of Co significantly facilitates CO₂ hydrogenation. The Co-BiOCl interface stabilizes the key CO* intermediate and significantly reduces the kinetic barrier to CH₂* formation, tuning the subsequent hydrogenation and C–C coupling into thermodynamically favorable exothermal processes. In the following steps, the hydrogenation of CH₂* to produce CH₃* and CH₄ are thermodynamically favorable, with –0.52 and –1.77 eV of energy emission, respectively. C–C coupling between CH₂* and CH₂* or between CH₃* and CH₃* naturally continues to generate C₂H₄ and C₂H₆. Therefore, the collective *in situ* DRIFTS and DFT results demonstrate that the introduction of Co into BiOCl contributes to spin-charge enrichment on Co-BiOCl surfaces, which helps stabilize reaction intermediates and promotes C–C coupling reactions (Fig. 7c).

4. Conclusions

In summary, spin-polarized BiOCl was synthesized by doping magnetic Co²⁺ ions in ultrathin BiOCl sheets. Co doping allows tailoring the products of photocatalytic CO₂ reduction on Co-BiOCl to CH₄, C₂H₄, and C₂H₆. When considering the experimental and theoretical results together, it is evident that CO₂ adsorption is enhanced by the incorporation of Co, resulting in a strong built-in electric field for charge separation and transfer. Importantly, the introduction of Co increases the spin-polarized charges and boosts CO adsorption on Co-BiOCl, thereby stabilizing reaction intermediates and promoting C–C coupling reactions. A positive effect of spin polarization on selective CO₂ photoreduction was also observed for Fe-BiOCl, Ni-BiOCl, and Cu-BiOCl. This work presents a BiOCl-based catalyst created by introducing spin polarization to regulate selective CO₂ conversion into hydrocarbon products, representing an effective strategy for enhancing photocatalytic CO₂ reduction in the future of solar-to-fuel conversion.

CRediT authorship contribution statement

Tingjiang Yan: Writing – review & editing, Visualization, Validation, Supervision, Resources, Project administration, Methodology, Investigation, Funding acquisition, Formal analysis, Data curation, Conceptualization. **Dapeng Zhang:** Supervision. **Na Li:** Supervision, Funding acquisition. **Fuzhi Zhang:** Methodology, Investigation. **Min Xu:** Methodology, Investigation. **Yuhua Wang:** Supervision, Software, Methodology. **Fu Tian:** Methodology, Investigation, Data curation. **Yipin Zhang:** Software, Methodology, Investigation, Formal analysis, Data curation. **Weiguang Ran:** Supervision, Software, Methodology. **Wenjuan Li:** Writing – review & editing, Writing – original draft,

Visualization, Validation, Supervision, Software, Resources, Project administration, Methodology, Investigation, Funding acquisition, Formal analysis, Data curation, Conceptualization.

Declaration of Competing Interest

The authors declare that they have no known competing financial interests or personal relationships that could have appeared to influence the work reported in this paper.

Data availability

The data that has been used is confidential.

Acknowledgements

This work is financially supported by National Natural Science Foundation of China (22172086, 22105117), the Major Basic Research Project of Shandong Province (ZR2021ZD06), Taishan Scholars Program of Shandong Province (NO. tsqn202103064), and Natural Science Foundation of Shandong Province (ZR2022MB078).

Appendix A. Supporting information

Supplementary data associated with this article can be found in the online version at doi:10.1016/j.apcatb.2024.123978.

References

- [1] Q. Wang, Z. Miao, Y. Zhang, T. Yan, L. Meng, X. Wang, Photocatalytic reduction of CO₂ with H₂O mediated by Ce-tailored bismuth oxybromide surface frustrated Lewis pairs, *ACS Catal.* 12 (2022) 4016–4025.
- [2] T. Kong, Y. Jiang, Y. Xiong, Photocatalytic CO₂ conversion: what can we learn from conventional CO_x hydrogenation? *Chem. Soc. Rev.* 49 (2020) 6579–6591.
- [3] X. Li, Y. Sun, J. Xu, Y. Shao, J. Wu, X. Xu, Y. Pan, H. Ju, J. Zhu, Y. Xie, Selective visible-light-driven photocatalytic CO₂ reduction to CH₄ mediated by atomically thin CuIn₅S₈ layers, *Nat. Energy* 4 (2019) 690–699.
- [4] Y. Pan, Y. You, S. Xin, Y. Li, G. Fu, Z. Cui, Y. Men, F. Cao, S. Yu, J.B. Goodenough, Photocatalytic CO₂ reduction by carbon-coated indium-oxide nanobelts, *J. Am. Chem. Soc.* 139 (2017) 4123–4129.
- [5] S. Si, H. Shou, Y. Mao, X. Bao, G. Zhai, K. Song, Z. Wang, P. Wang, Y. Liu, Z. Zheng, Y. Dai, L. Song, B. Huang, H. Cheng, Low-coordination single Au atoms on ultrathin ZnIn₂S₄ nanosheets for selective photocatalytic CO₂ reduction towards CH₄, *Angew. Chem. Int. Ed.* 61 (2022) 22209446.
- [6] J. Li, H. Huang, W. Xue, K. Sun, X. Song, C. Wu, L. Nie, Y. Li, C. Liu, Y. Pan, H. Jiang, D. Mei, C. Zhong, Self-adaptive dual-metal-site pairs in metal-organic frameworks for selective CO₂ photoreduction to CH₄, *Nat. Catal.* 4 (2021) 719–729.
- [7] L. Cheng, X. Yue, J. Fan, Q. Xiang, Site-specific electron-driving observations of CO₂-to-CH₄ photoreduction on Co-doped CeO₂/crystalline carbon nitride S-scheme heterojunctions, *Adv. Mater.* 34 (2022) 2200929.
- [8] T. Yan, N. Li, L. Wang, W. Ran, P.N. Duchesne, L. Wan, N. Nhat Truong, L. Wang, M. Xia, G.A. Ozin, Bismuth atom tailoring of indium oxide surface frustrated Lewis pairs boosts heterogeneous CO₂ photocatalytic hydrogenation, *Nat. Commun.* 11 (2020) 6095.
- [9] W. Shangguan, Q. Liu, Y. Wang, N. Sun, Y. Liu, R. Zhao, Y. Li, C. Wang, J. Zhao, Molecular-level insight into photocatalytic CO₂ reduction with H₂O over Au nanoparticles by interband transitions, *Nat. Commun.* 13 (2022) 3894.
- [10] T. Xie, S. Sun, J. Xu, Y. Luo, J. Cui, Purposefully designing Co-S-codoping in hierarchical BiOCl architectures and elucidating the mechanism for enhanced visible-light-driven photocatalytic activity, *Appl. Surf. Sci.* 604 (2022) 154582.
- [11] X. Yang, S. Sun, J. Cui, M. Yang, Y. Luo, S. Liang, Synthesis, functional modifications, and diversified applications of hybrid BiOCl-based heterogeneous photocatalysts: a review, *Cryst. Growth Des.* 21 (2021) 6576–6618.
- [12] S. Tao, S. Sun, T. Zhao, J. Cui, M. Yang, X. Yu, Q. Yang, X. Zhang, S. Liang, One-pot construction of Ta-doped BiOCl/Bi heterostructures toward simultaneously promoting visible light harvesting and charge separation for highly enhanced photocatalytic activity, *Appl. Surf. Sci.* 543 (2021) 148798.
- [13] L. Wang, X. Zhao, D. Lv, C. Liu, W. Lai, C. Sun, Z. Su, X. Xu, W. Hao, S. Dou, Y. Du, Promoted photocharge separation in 2D lateral epitaxial heterostructure for visible-light-driven CO₂ photoreduction, *Adv. Mater.* 32 (2020) 2004311.
- [14] X. Zhao, Y. Xia, H. Li, X. Wang, J. Wei, X. Jiao, D. Chen, Oxygen vacancy dependent photocatalytic CO₂ reduction activity in liquid-exfoliated atomically thin BiOCl nanosheets, *Appl. Catal. B* 297 (2021) 120426.
- [15] Y. Shi, J. Li, C. Mao, S. Liu, X. Wang, X. Liu, S. Zhao, X. Liu, Y. Huang, L. Zhang, Van Der Waals gap-rich BiOCl atomic layers realizing efficient, pure-water CO₂-to-CO photocatalysis, *Nat. Commun.* 12 (2021) 5923.

[16] Y. Zhang, Z. Xu, Q. Wang, W. Hao, X. Zhai, X. Fei, X. Huang, Y. Bi, Unveiling the activity origin of ultrathin BiOCl nanosheets for photocatalytic CO₂ reduction, *Appl. Catal. B* 299 (2021) 120679.

[17] S. Cheng, Z. Sun, K. Lim, T. Zhang, E. Hondo, T. Du, L. Liu, M. Judd, N. Cox, Z. Yin, G. Li, S. Kawi, BiOCl nanoflowers with high levels of oxygen vacancy for photocatalytic CO₂ reduction, *ACS Appl. Nano Mater.* 6 (2023) 3608–3617.

[18] Y. Wang, H. Wang, L. Guo, T. He, Boosting the photocatalytic CO₂ reduction reaction over BiOCl nanosheet via Cu modification, *J. Colloid Interface Sci.* 648 (2023) 889–897.

[19] L. Wang, R. Wang, T. Qiu, L. Yang, Q. Han, Q. Shen, X. Zhou, Y. Zhou, Z. Zou, Bismuth vacancy-induced efficient CO₂ photoreduction in BiOCl directly from natural air: a progressive step toward photosynthesis in nature, *Nano Lett.* 21 (2021) 10260–10266.

[20] Z. Zhang, R. Guo, J. Tang, Y. Miao, J. Gu, W. Pan, Fabrication of Bi-BiOCl/MgIn₂S₄ heterostructure with step-scheme mechanism for carbon dioxide photoreduction into methane, *J. CO₂ Util.* 45 (2021) 101453.

[21] X. Ren, M. Gao, Y. Zhang, Z. Zhang, X. Cao, B. Wang, X. Wang, Photocatalytic reduction of CO₂ on BiOX: effect of halogen element type and surface oxygen vacancy mediated mechanism, *Appl. Catal. B* 274 (2020) 119063.

[22] K. Yan, L. Chen, Y. Hu, T. Wang, C. Chen, C. Gao, Y. Huang, B. Li, Accelerating solar driven CO₂ reduction via sulfur-doping boosted water dissociation and proton transfer, *Nano Res.* (2023), <https://doi.org/10.1007/s12274-023-5888-3>.

[23] Z. Huang, J. Wu, M. Ma, J. Wang, S. Wu, X. Hu, C. Yuan, Y. Zhou, The selective production of CH₄ via photocatalytic CO₂ reduction over Pd-modified BiOCl, *N. J. Chem.* 46 (2022) 16889–16898.

[24] W. Wang, C. Deng, S. Xie, Y. Li, W. Zhang, H. Sheng, C. Chen, J. Zhao, Photocatalytic C–C coupling from carbon dioxide reduction on copper oxide with mixed-valence copper(I)/copper(II), *J. Am. Chem. Soc.* 143 (2021) 2984–2993.

[25] E.V. Kondratenko, G. Mul, J. Baltrusaitis, G.O. Larrazábal, J. Pérez-Ramírez, Status and perspectives of CO₂ conversion into fuels and chemicals by catalytic, photocatalytic and electrocatalytic processes, *Energy Environ. Sci.* 6 (2013) 3112–3135.

[26] C. Lin, T. Liu, S. Lin, K.M. Boopathi, C. Chiang, W. Tzeng, W.C. Chien, H. Hsu, C. Luo, H. Tsai, H. Chen, P. Kuo, J. Shihue, J. Chiou, W. Pong, C. Chen, C. Chen, Spin-polarized photocatalytic CO₂ reduction of Mn-doped perovskite nanoplates, *J. Am. Chem. Soc.* 144 (2022) 15718–15726.

[27] Y. Gong, W. Zhong, Y. Li, Y. Qiu, L. Zheng, J. Jiang, H. Jiang, Regulating photocatalysis by spin-state manipulation of cobalt in covalent organic frameworks, *J. Am. Chem. Soc.* 142 (2020) 16723–16731.

[28] D. Wu, H. Yin, Z. Wang, M. Zhou, C. Yu, J. Wu, H. Miao, T. Yamamoto, W. Zhaxi, Z. Huang, L. Liu, W. Huang, W. Zhong, Y. Einaga, J. Jiang, Z. Zhang, Spin manipulation in a metal–organic layer through mechanical exfoliation for highly selective CO₂ photoreduction, *Angew. Chem. Int. Ed.* 62 (2023) 202301925.

[29] C. Wang, Y. Zhang, W. Wang, D. Pei, G. Huang, J. Chen, X. Zhang, H. Yu, Enhanced photocatalytic degradation of bisphenol A by Co-doped BiOCl nanosheets under visible light irradiation, *Appl. Catal. B* 221 (2018) 320–328.

[30] J. Liu, H. Wang, M. Chang, M. Sun, C. Zhang, L. Yang, H. Du, Z. Luo, Facile synthesis of BiOCl with extremely superior visible light photocatalytic activity synergistically enhanced by Co doping and oxygen vacancies, *Sep. Purif. Technol.* 301 (2022) 121953.

[31] X. Gao, C. Gong, X. Wang, W. Zhu, Y. Luo, Facile synthesis of cobalt doped BiOCl ultrathin nanosheets as superior photocatalyst for degradation of carbamazepine under visible light, *J. Solid State Chem.* 298 (2021) 122131.

[32] Z. Wu, J. Shen, W. Li, J. Li, D. Xia, D. Xu, S. Zhang, Y. Zhu, Electron self-sufficient core-shell BiOCl@Fe-BiOCl nanosheets boosting Fe (III)/Fe(II) recycling and synergistic photocatalysis-Fenton for enhanced degradation of phenol, *Appl. Catal. B* 330 (2023) 122642.

[33] P. Attri, P. Garg, M. Chauhan, R. Singh, R.K. Sharma, S. Kumar, D. Lim, G. R. Chaudhary, Metal doped BiOCl nano-architectures (M-BiOCl, M =Ni, Mo, Cd, Co) for efficient visible light photocatalytic and antibacterial behaviour, *J. Environ. Chem. Eng.* 11 (2023) 109498.

[34] W. Ran, H.M. Noh, S.H. Park, B.R. Lee, J.H. Kim, J.H. Jeong, J. Shi, Er³⁺-Activated NaLaMgWO₆ double perovskite phosphors and their bifunctional application in solid-state lighting and non-contact optical thermometry, *Dalton Trans.* 48 (2019) 4405.

[35] M. Guan, C. Xiao, J. Zhang, S. Fan, R. An, Q. Cheng, J. Xie, M. Zhou, B. Ye, Y. Xie, Vacancy associates promoting solar-driven photocatalytic activity of ultrathin bismuth oxychloride nanosheets, *J. Am. Chem. Soc.* 135 (2013) 10411–10417.

[36] R. Zhang, R. Chiliverry, D. Yao, W. Chen, F. Lu, W. Gao, Y. Fang, Z. Zhong, Y. Song, Controlled engineering of tunable 3D-BiOX (X = Cl, Br) hierarchical nanostructures via dopamine-mediated synergistic interactions for efficient visible-light absorption photocatalysis, *Appl. Surf. Sci.* 574 (2022) 151683.

[37] Y. Yang, G. Zeng, D. Huang, C. Zhang, D. He, C. Zhou, W. Wang, W. Xiong, B. Song, H. Yi, S. Ye, X. Ren, In situ grown single-atom cobalt on polymeric carbon nitride with bidentate ligand for efficient photocatalytic degradation of refractory antibiotics, *Small* 16 (2020) 2001634.

[38] J. Di, C. Chen, S. Yang, S. Chen, M. Duan, J. Xiong, C. Zhu, R. Long, W. Hao, Z. Chi, H. Chen, Y. Weng, J. Xia, L. Song, S. Li, H. Li, Z. Liu, Isolated single atom cobalt in Bi₂O₄Br atomic layers to trigger efficient CO₂ photoreduction, *Nat. Commun.* 10 (2019) 2840.

[39] G. Li, X. Sun, P. Chen, M. Song, T. Zhao, F. Liu, S. Yin, Insights into spin polarization regulated exciton dissociation and charge separation of C₃N₄ for efficient hydrogen evolution and simultaneous benzylamine oxidation, *Nano Res.* 16 (2023) 8845–8852.

[40] B. Fang, Z. Xing, W. Kong, Z. Li, W. Zhou, Electron spin polarization-mediated charge separation in Pd/CoP@CoNiP superstructures toward optimized photocatalytic performance, *Nano Energy* 101 (2022) 107616.

[41] H. Li, G. Wang, Q. Deng, W. Hu, W. Hou, Metal-alcohol coordination promoted reduction of bismuth(III) in bismuth-based semiconductors for enhanced photocatalytic activity, *Appl. Catal. B* 344 (2024) 123652.

[42] X. Zhou, F. Yan, S. Wu, B. Shen, H. Zeng, J. Zhai, Remarkable piezophoto coupling catalysis behavior of BiOX/BaTiO₃ (X = Cl, Br, Cl_{0.166}Br_{0.834}) piezoelectric composites, *Small* 16 (2020) 2001573.

[43] J. Jing, J. Yang, Z. Zhang, Y. Zhu, Supramolecular zinc porphyrin photocatalyst with strong reduction ability and robust built-in electric field for highly efficient hydrogen production, *Adv. Energy Mater.* 11 (2021) 2101392.

[44] P. Liu, Y. Men, X. Meng, C. Peng, Y. Zhao, Y. Pan, Electronic interactions on platinum/(metal-oxide)-based photocatalysts boost selective photoreduction of CO₂ to CH₄, *Angew. Chem. Int. Ed.* 62 (2023) 202309443.

[45] P. Liu, Z. Huang, X. Gao, X. Hong, J. Zhu, G. Wang, Y. Wu, J. Zeng, X. Zheng, Synergy between palladium single atoms and nanoparticles via hydrogen spillover for enhancing CO₂ photoreduction to CH₄, *Adv. Mater.* 34 (2022) 2200057.

[46] K. Wang, J. Lu, Y. Lu, C. Lau, Y. Zheng, X. Fan, Unravelling the C-C coupling in CO₂ photocatalytic reduction with H₂O on Au/TiO_{2-x}: Combination of plasmonic excitation and oxygen vacancy, *Appl. Catal. B* 292 (2021) 120147.

[47] Y. Zhang, X. Zhi, J.R. Harmer, H. Xu, K. Davey, J. Ran, S. Qiao, Facet-specific active surface regulation of Bi_xMO_y (M=Mo, V, W) nanosheets for boosted photocatalytic CO₂ reduction, *Angew. Chem. Int. Ed.* 61 (2022) 202212355.

[48] S. Chakraborty, R. Das, M. Riyaz, K. Das, A. Singh, D. Bagchi, C.P. Vinod, S. Peter, Wurtzite CuGaS₂ with an in-situ-formed CuO layer photocatalyzes CO₂ conversion to ethylene with high selectivity, *Angew. Chem. Int. Ed.* 62 (2023) 202216613.

[49] S. Ning, H. Ou, Y. Li, C. Lv, S. Wang, D. Wang, J. Ye, Co⁰–Co⁸⁺ interface double-site-mediated C–C coupling for the photothermal conversion of CO₂ into light olefins, *Angew. Chem. Int. Ed.* 62 (2023) 202302253.

[50] W. Li, Y. Zhang, Y. Wang, W. Ran, Q. Guan, W. Yi, L. Zhang, D. Zhang, N. Li, T. Yan, Graphdiyne facilitates photocatalytic CO₂ hydrogenation into C₂₊ hydrocarbons, *Appl. Catal. B* 340 (2024) 123267.

[51] Z. Han, W. Qian, H. Zhang, H. Ma, Q. Sun, W. Ying, Effect of rare-earth promoters on precipitated iron-based catalysts for Fischer–Tropsch synthesis, *Ind. Eng. Chem. Res.* 59 (2020) 14598–14605.

[52] W. Qian, H. Ma, X. Wu, H. Zhang, Z. Han, Q. Sun, W. Ying, Study of the Fischer–Tropsch synthesis on nano precipitated iron-based catalysts with different particle sizes, *RSC Adv.* 10 (2020) 42903.

[53] F.Y. Xu, K. Meng, B.C. Zhu, H.B. Liu, J.S. Xu, J.G. Yu, Graphdiyne: a new photocatalytic CO₂ reduction cocatalyst, *Adv. Funct. Mater.* 29 (2019) 1904256.

[54] D. Zhou, X. Xue, X. Wang, Q. Luan, A. Li, L. Zhang, B. Li, W. Dong, G. Wang, C. Hou, Ni, In co-doped ZnIn₂S₄ for efficient hydrogen evolution: Modulating charge flow and balancing H adsorption/desorption, *Appl. Catal. B* 310 (2022) 121337.

[55] L. Wang, B. Zhao, C. Wang, M. Sun, Y. Yu, B. Zhang, Thermally assisted photocatalytic conversion of CO₂–H₂O to C₂H₄ over carbon doped In₂S₃ nanosheets, *J. Mater. Chem. A* 8 (2020) 10175–10179.

[56] H. Ou, G. Li, W. Ren, B. Pan, G. Luo, Z. Hu, D. Wang, Y. Li, Atomically dispersed Au-assisted C–C coupling on red phosphorus for CO₂ photoreduction to C₂H₆, *J. Am. Chem. Soc.* 144 (2022) 22075–22082.